Journal of Marine Science and Engineering

MDPI

Article

Inlet Passage Hydraulic Performance Optimization of Coastal Drainage Pump System Based on Machine Learning Algorithms

Tao Jiang [1], Weigang Lu [1,*], Linguang Lu [1], Lei Xu [1], Wang Xi [1,2,3], Jianfeng Liu [1] and Ye Zhu [4]

[1] College of Hydraulic Science and Engineering, Yangzhou University, Yangzhou 225009, China; dx120210102@stu.yzu.edu.cn (T.J.)
[2] High-Tech Key Laboratory of Agricultural Equipment and Intelligence of Jiangsu Province, Jiangsu University, Zhenjiang 212000, China
[3] Asia Pacific Pump Valve Co., Ltd., Taizhou 225300, China
[4] Changzhou Urban Flood Control Engineering Management Office, Changzhou 213000, China
* Correspondence: wglu@yzu.edu.cn

Abstract: The axial-flow pump system has been widely applied to coastal drainage pump stations, but the hydraulic performance optimization based on the contraction angles of the inlet passage has not been studied. This paper combined the computational fluid dynamics (CFD) method, machine learning (ML) algorithms and genetic algorithm (GA) to find the optimal contraction angles of the inlet passage. The 125 sets of comprehensive objective function were obtained by the CFD method. Three contraction angles and comprehensive objective function values were regressed by three ML algorithms. After hyperparameter optimization, the Gaussian process regression (GPR) model had the highest $R^2 = 0.958$ in the test set and had the strongest generalization ability among the three models. The impact degree of the three contraction angles on the objective function of the GPR model was investigated by the Sobol sensitivity analysis method; the results indicated that the order of impact degree from high to low was $\theta_3 > \theta_2 > \theta_1$. The optimal objective function values of the GPR model and corresponding contraction angles were searched through GA; the maximum objective function value was 0.963 and corresponding contraction angles were $\theta_1 = 13.34°$, $\theta_2 = 28.36°$ and $\theta_3 = 3.64°$, respectively. The results of this study can provide reference for the optimization of inlet passages in coastal drainage pump systems.

Keywords: coastal drainage pump system; inlet passage optimization; computational fluid dynamics method; machine learning algorithms; sobol sensitivity analysis; genetic algorithm

Academic Editor: Giuseppe Giorgi

Received: 8 January 2025
Revised: 24 January 2025
Accepted: 27 January 2025
Published: 31 January 2025

Citation: Jiang, T.; Lu, W.; Lu, L.; Xu, L.; Xi, W.; Liu, J.; Zhu, Y. Inlet Passage Hydraulic Performance Optimization of Coastal Drainage Pump System Based on Machine Learning Algorithms. *J. Mar. Sci. Eng.* **2025**, *13*, 274. https://doi.org/10.3390/jmse13020274

1. Introduction

With the development of axial-flow pumps, the axial-flow pump systems are increasingly used in coastal drainage pump stations and marine jet propulsion plants [1,2]. The axial-flow pump system generally includes the inlet passage, impeller, guide vane and outlet passage (Figure 1), and the function of the inlet passage is to uniformly direct the water from the inlet sump to impeller chamber and provide a good flow condition for the impeller inlet [3]. For a low-head axial-flow pump system, the suction vortex in the inlet passage can cause vibration of the impeller, seriously affecting its operation [4].

Moreover, the efficiency of the pump system can be improved more than 5% after optimizing the flow passage [5]. Therefore, the hydraulic performance of the inlet passage has a great effect on the stability and efficiency of the pump system.

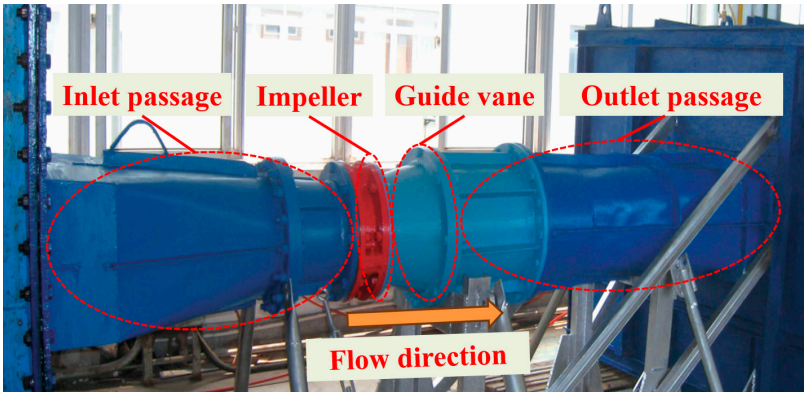

Figure 1. Components of pump system.

Many authors have studied the hydraulic performance of the axial-flow pump system. In energy loss, the entropy production theory was adopted to analyze the energy dissipation distribution of the components of the axial-flow pump system under different flow rates and the reasons were analyzed for the production of high entropy production areas [6,7]. In cavitation, the condition of ensuring erosion-free flow in the impeller of an axial pump with a specific speed of 600 was studied, and the results indicated that the condition ensures the ratio $NPSH_a/NPSH_a3 > 2.5$ [8]. In addition, the tip leakage vortex (TLV) of the axial flow pump was studied, indicating that the variations in the vortex structure will generate and promote the development of cavitation [9]. In pressure fluctuation, the pressure fluctuation characteristics of the axial-flow pump with different flow rates and positions were studied, and the time-domain and frequency-domain characteristics of pressure fluctuation were analyzed [10,11]. In the vortex, the vortex at the inlet of the axial-flow pump has been studied through experiments and CFD methods, and the influence mechanism of the vortex on pump operation has been revealed [12,13].

In order to save costs and improve optimization efficiency, the hydraulic performance of pump passage optimization is usually predicted through the CFD method. The mechanisms of energy dissipation in the passage of a pump as turbine (PAT) were studied by the CFD method, revealing that the blade inlet shock, flow deviation at the blade outlet, flow separation, backflow and vortices in flow passages are categorized as the main reasons for entropy production [14]. The influence of the splitter blade on a special impeller used in the PAT was studied by the CFD method, displaying that adding splitter blades can obviously increase its hydraulic performance under large flow conditions [15]. In addition to basic analysis of the flow state, the researchers have also studied the energy loss [16–19], cavitation [20], pressure fluctuation [21], impeller forces [22] and hydrodynamic characteristics of a full working condition [23], etc., through the CFD method.

With the development of artificial intelligence (AI), machine learning (ML) algorithms are widely used in the optimization of pump systems. In the optimization process of a pump system, ML algorithms are usually used as surrogate models, which receive data entirely from the CFD calculation [24]. The heat transfer rate was predicted to speed up the calculation process during the channel optimization through artificial neural network models and genetic algorithm [25]. In the axial-flow pump, the machine learning algorithms were used in blade optimization to improve the hydraulic performance of the axial-flow pump in different working conditions [26,27]. In the

centrifugal pump, the machine learning algorithms were applied in different aspects including hydraulic performance prediction [28,29], rotating stall [30,31], structural optimization [32,33], cavitation optimization [34], etc. In the heat pump system, its performance was predicted with high precision by machine learning algorithms [35,36].

In this paper, the inlet passage designed by three contraction angles (θ_1, θ_2 and θ_3) was optimized for better hydraulic performance through the CFD method, three different machine learning algorithms and the genetic algorithm. The flowchart of this study is shown in Figure 2, and the steps of this study are as follows: Step 1, design 125 sets of inlet passages schemes by changing the three contraction angles based on constraint conditions. Step 2, solve the hydraulic performance of 125 sets of inlet passages by the CFD method which has been verified through the model test, and calculate the comprehensive objective function (Y) by the information weight method. Step 3, after hyperparameter optimization by the Bayesian optimization method, establish three machine learning regression models for three contraction angles and the comprehensive objective function, choose the optimal regression model (GPR model) based on the generalization ability of models in the test set, and analyze the influence degree of three contraction angles on the objective function. Step 4, search for the optimal inlet passage scheme corresponding to the highest objective function value by the genetic algorithm, and compare the CFD cloud map results of the initial scheme and optimal scheme.

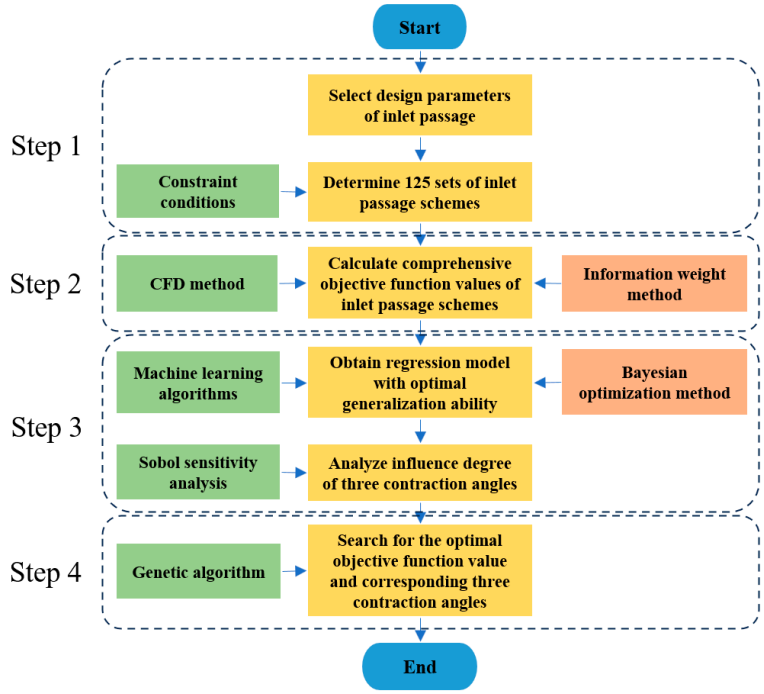

Figure 2. Flowchart of this study.

2. Research Object and Method

2.1. Research Object

The research object of this paper is the inlet passage of an axial-flow pump system. The flow state in the inlet passage is the contraction flow, so the contraction angle of a circular segment on the horizontal plane (θ_1), the contraction angle of a square to circular segment on the horizontal plane (θ_2) and the contraction angle on the vertical plane (θ_3) were researched to explore the effect of three contraction angles on the hydraulic performance of the inlet passage and search optimal hydraulic performance scheme of the inlet passage. The model dimension of the inlet passage and axial pump are shown in Figure 3. The inlet passage is divided into three parts: square segment, square to circular segment and circular segment. The model perspective drawing of inlet passage is shown in Figure 4.

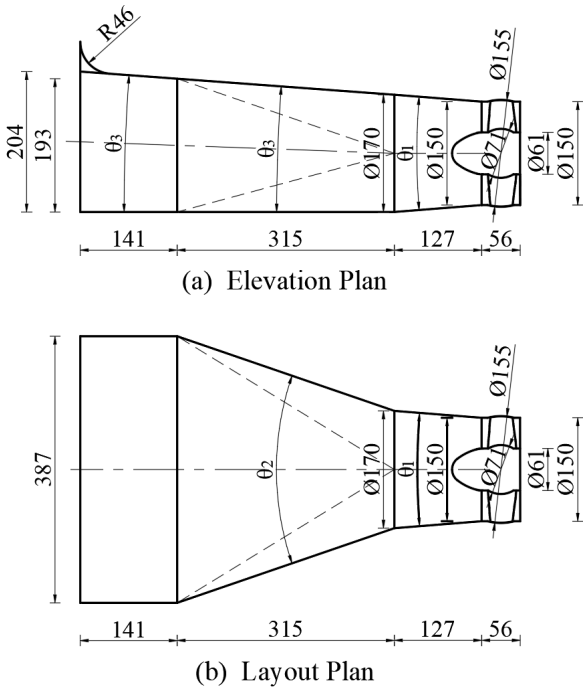

Figure 3. Model dimension of inlet passage and axial pump (unit: mm).

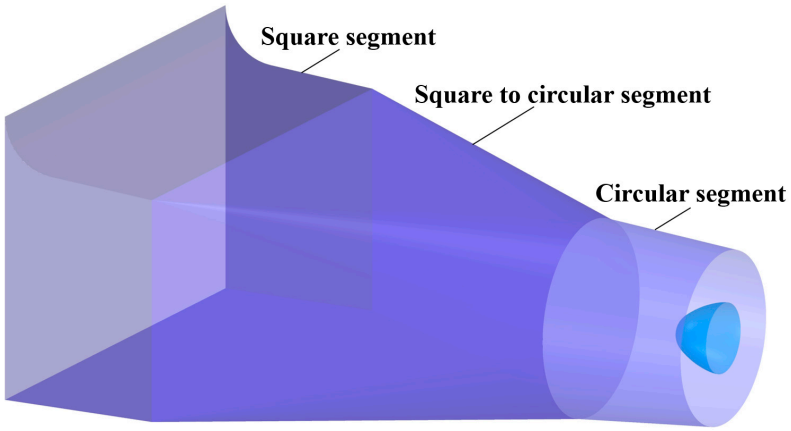

Figure 4. Model perspective drawing of inlet passage.

2.2. Research Method

2.2.1. Numerical Simulation Method

The flow in the inlet passage is a three-dimensional incompressible flow. The flow can be described by the conservation of mass equation and conservation of momentum equation (Navier–Stokes equation), to better solve the equations. The Reynolds Average Navier–Stokes equation is introduced, thus, two equations are as below.

$$\frac{\partial \overline{u_i}}{\partial x_i} = 0 \tag{1}$$

$$\rho \frac{\partial \overline{u_i}}{\partial t} + \rho \frac{\partial \overline{u_i}\,\overline{u_j}}{\partial x_j} = -\frac{\partial \overline{p}}{\partial x_i} + \frac{\partial}{\partial x_j}\left[\mu\left(\frac{\partial \overline{u_i}}{\partial x_j} + \frac{\partial \overline{u_j}}{\partial x_i}\right) - \rho\overline{u_i' u_j'}\right] + F_i \tag{2}$$

where u_i, u_j are velocity components, x_i, x_j are coordinate direction, t is time, p is pressure, μ is dynamic viscosity, F_i is gravity force and $-\rho\overline{u_i' u_j'}$ is Reynolds stress.

To close the time-averaged equations, the turbulent model is added. The Re-normalization Group (RNG) $k-\varepsilon$ turbulent model has been widely used in the numerical simulation of the pump passage and gained good calculation results [37,38], so the RNG $k-\varepsilon$ turbulent model is adopted in this paper. The transport equations and corresponding coefficient to solve k and ε are as below.

$$\rho \frac{\partial k}{\partial t} + \rho \frac{\partial k\overline{u_i}}{\partial x_i} = \frac{\partial}{\partial x_j}\left[\alpha_k (\mu + \mu_t)\frac{\partial k}{\partial x_j}\right] + G_k + \rho\varepsilon \tag{3}$$

$$\rho \frac{\partial \varepsilon}{\partial t} + \rho \frac{\partial \varepsilon\overline{u_i}}{\partial x_i} = \frac{\partial}{\partial x_j}\left[\alpha_\varepsilon (\mu + \mu_t)\frac{\partial \varepsilon}{\partial x_j}\right] + \frac{C_{1\varepsilon}^{*}\varepsilon}{k} G_k - C_{2\varepsilon}\rho\frac{\varepsilon^2}{k} \tag{4}$$

where

$$\alpha_k = \alpha_\varepsilon = 1.39, \quad C_{2\varepsilon} = 1.68 \tag{5}$$

$$G_k = \mu_t\left(\frac{\partial \overline{u_i}}{\partial x_j} + \frac{\partial \overline{u_j}}{\partial x_i}\right)\frac{\partial \overline{u_i}}{\partial x_j} \tag{6}$$

$$C_{1\varepsilon}^{*} = C_{1\varepsilon} - \frac{\eta(1-\eta/\eta_0)}{1+\beta\eta^3} \tag{7}$$

In Equation (7), the corresponding coefficients and variables are as below.

$$C_{1\varepsilon} = 1.42, \quad \eta_0 = 4.377, \quad \beta = 0.012 \tag{8}$$

$$\eta = (2E_{ij}\cdot E_{ij})^{1/2}\frac{k}{\varepsilon} \tag{9}$$

$$E_{ij} = \frac{1}{2}\left(\frac{\partial \overline{u_i}}{\partial x_j} + \frac{\partial \overline{u_j}}{\partial x_i}\right) \tag{10}$$

2.2.2. Machine Learning Algorithms

Gaussian Process Regression

The Gaussian process (GP) is a set of any finite number of random variables with a joint Gaussian distribution, and its properties are entirely determined by the mean function and covariance function,

$$\begin{cases} m(x) = E[f(x)] \\ k(x,x') = E[(f(x) - m(x))(f(x') - m(x'))] \end{cases} \tag{11}$$

where $x, x' \in R^d$ are random variables.

Therefore, the GP can be defined as $f(x) \sim \mathrm{GP}(m(x), k(x,x'))$. For regression problems, the following regression can be considered,

$$y = f(x) + \varepsilon \tag{12}$$

where x is input value, $f(x)$ is true value, ε is error term and y is observed value.

Further, assume that the error ε satisfies $\varepsilon \sim N(0, \sigma^2)$, the prior distribution of the observed value y can be obtained as

$$y \sim N(0, K(X,X) + \delta_n^2 I_n) \tag{13}$$

The joint prior distribution of observed and predicted values is

$$\begin{bmatrix} y \\ f_* \end{bmatrix} \sim N\left(0, \begin{bmatrix} K(X,X) + \delta_n^2 I_n & K(X,x_*) \\ K(x_*,X) & k(x_*,x_*) \end{bmatrix}\right) \tag{14}$$

where $K(X,X)$ is $n \times n$ symmetric positive definite covariance matrix, $K(X,x_*) = K(X,x_*)^{\mathrm{T}}$ is $n \times 1$ covariance matrix between the test point x_* and the input of training set X, $k(x_*,x_*)$ is the covariance matrix of the test point x_* and I_n is the n identity matrix.

Therefore, the posterior distribution of the predicted values can be calculated as

$$f_* \mid X, y, x_* \sim N\left(\bar{f}_*, cov(f_*)\right) \tag{15}$$

where

$$\bar{f}_* = K(x_*,X)[K(X,X) + \delta_n^2 I_n]^{-1} y \tag{16}$$

$$cov(f_*) = k(x_*,x_*) - K(x_*,X) \times [K(X,X) + \delta_n^2 I_n]^{-1} K(X,x_*) \tag{17}$$

Then, $\hat{\mu}_* = \bar{f}_*$ and $\hat{\sigma}_{f_*}^2 = cov(f_*)$ are the mean and variance of the predicted values f_* corresponding to the test points x_*, respectively.

Feedforward Neural Network

A feedforward neural network (FNN) performs well in the regression of nonlinear functions. It consists of an input layer, one or more hidden layers and an output layer. Each layer of the FNN contains several neurons. In the FNN, the relationship between the input and output of each neuron is

$$I_j^k = \sum_{i=1}^{n} \omega_{j,i}^k O_i^{k-1} + b_j^k \tag{18}$$

$$O_j^k = f\left(I_j^k\right) \tag{19}$$

where I_j^k is the input of the jth neuron in the kth layer, O_j^k is output of the jth neuron in the kth layer, O_i^{k-1} is output of the ith neuron in the $(k-1)$th layer, n is the number of neurons in the $(k-1)$th layer, $\omega_{j,i}^k$ is the connection weight between ith neuron in the $(k-1)$th layer and jth neuron in the kth layer, b_j^k is the bias of jth neuron in the kth layer and f is the activation function.

The learning process of the FNN consists of the forward propagation of signals and back propagation of errors. When the output of forward propagation does not reach the true value, the error between the predicted value and the true value is backpropagated to correct connection weights and biases. Through repeated iterations of forward propagation and back propagation, the error L is minimized. The error L is

$$L = \frac{1}{2}\sum_{a=1}^{m}(y_a - \hat{y}_a)^2 \tag{20}$$

where m is the number of neurons in output layer, y_a is the true value and $\hat{y}_a$ is the predictive value.

The corrected connection weight $\omega_{j,i}^{k}{}'$ and bias $b_j^{k\prime}$ are calculated according to the following formulas,

$$\omega_{j,i}^{k}{}' = \omega_{j,i}^{k} - \eta\frac{\partial L}{\partial \omega_{j,i}^{k}} \tag{21}$$

$$b_j^{k\prime} = b_j^{k} - \eta\frac{\partial L}{\partial b_j^{k}} \tag{22}$$

where $\omega_{j,i}^{k}{}'$ is the corrected connection weight between the ith neuron in the $(k-1)$th layer and jth neuron in the kth layer, $b_j^{k\prime}$ is corrected bias of the jth neuron in the kth layer and η is the learning rate.

Support Vector Regression

Support Vector Regression (SVR) is a regression method based on Support Vector Machine (SVM). The SVR uses the kernel function to nonlinearly map the raw data to a high-dimensional space and finds a hyperplane in that space to minimize the difference between the projection of the input data on the hyperplane and the target value. This hyperplane is a regression function of SVR, and the SVR can be formalized as follows:

$$\min_{\omega,b}\frac{1}{2}\|\omega\|^2 + C\sum_{i=1}^{m} l_\epsilon(f(x_i) - y_i) \tag{23}$$

$$l_\epsilon(f(x_i) - y_i) = \begin{cases} 0, \text{if} |f(x_i) - y_i| \le \epsilon \\ |f(x_i) - y_i| - \epsilon, \text{otherwise} \end{cases} \tag{24}$$

where C is regularization constant and l_ϵ is ϵ-insensitive loss.

By introducing the relaxation variables ξ_i and $\hat{\xi}_i$, Equation (25) can be obtained,

$$\min_{\omega,b,\xi_i\hat{\xi}_i}\frac{1}{2}\|\omega\|^2 + C\sum_{i=1}^{m}\left(\xi_i + \hat{\xi}_i\right) \tag{25}$$

$$s.t.\begin{cases} f(x_i) - y_i \le \epsilon + \xi_i \\ y_i - f(x_i) \le \epsilon + \hat{\xi}_i \\ \xi_i \ge 0, \hat{\xi}_i \ge 0\,, i = 1,2,\dots,m \end{cases} \tag{26}$$

By introducing Lagrange multipliers, the dual formula of SVR is obtained,

$$\max_{\alpha,\hat{\alpha}}\sum_{i=1}^{m} y_i(\hat{a}_i - \alpha_i) - \epsilon(\hat{a}_i + \alpha_i) - \frac{1}{2}\sum_{i=1}^{m}\sum_{j=1}^{m}(\hat{a}_i - \alpha_i)\left(\hat{a}_j - \alpha_j\right)x_i^T x_j \tag{27}$$

$$s.t.\begin{cases} \sum_{i=1}^{m}(\hat{a}_i - \alpha_i) = 0 \\ 0 \le \alpha_i, \hat{a}_i \le C \end{cases} \tag{28}$$

The Karush–Kuhn–Tucker (KKT) condition needs to be met during the above process, that is,

$$\begin{cases} \alpha_i(f(x_i) - y_i - \epsilon - \xi_i) = 0 \\ \hat{\alpha}_i\left(y_i - f(x_i) - \epsilon - \hat{\xi}_i\right) = 0 \\ \alpha_i\hat{\alpha}_i = 0\,, \xi_i\hat{\xi}_i = 0 \\ (C - \alpha_i)\xi_i = 0, (C - \hat{a}_i)\hat{\xi}_i = 0 \end{cases} \tag{29}$$

The function used to predict new values can be expressed as

$$f(x) = \sum_{i=1}^{m}(\hat{a}_i - \alpha_i)\kappa(x,\ x_i) + b \tag{30}$$

where b is constant and $\kappa(x,\ x_i)$ is the kernel function.

2.2.3. Genetic Algorithm

The genetic algorithm is an adaptive and global probability search algorithm that simulates the genetic and evolutionary process of survival of the fittest in the natural environment. It starts with a population representing the potential solution set of the problem, first mapping the phenotype to the genotype, i.e., encoding, thereby mapping the solution space to the encoding space, with each encoding corresponding to a solution of the problem, called a chromosome or individual. After the initial population is generated, according to the principles of the fittest survival, it evolves its generation to produce increasingly better approximate solutions. In each generation, individuals are selected based on their fitness in the problem domain, and natural genetic operators are used for combination crossover and mutation to generate a population representing a new solution set. This process makes the population evolve like natural evolution, and the offspring population is more adapted to the environment than the previous generation, and the optimal individual in the last generation population can be decoded as an approximate optimal solution to the problem.

3. Verification of Numerical Simulation Result

3.1. Numerical Simulation

3.1.1. Boundary Conditions and Calculation Settings

The boundary conditions of calculation domains are shown in Figure 5. The calculation domains consisted of the inlet sump, inlet passage and outlet straight pipe. The mass-flow inlet boundary condition (0.038 m^3/s) was set at the inlet of the inlet sump, and it was 1.5 m away from the inlet of the inlet passage. The outflow boundary condition was set at the outlet of the outlet straight pipe, and the distance between the outflow boundary and the outlet of the inlet passage was twice the diameter of the outlet straight pipe to ensure the fully developed flow at the outlet of the calculation domains. Based on the rigid-lid approximation, the free water surface of the inlet sump was set as a symmetry boundary condition. Except for the above surfaces, all other surfaces of the calculation domains were set as wall boundary conditions, and the no-slip wall condition was adopted.

The calculation medium was set to water, the water density was set to 998.2 kg/m^3 and the water dynamic viscosity was set to 0.001 kg/(m·s). The magnitude of the gravitational acceleration was set to 9.81 m^2/s, with a vertical downward direction. The solving algorithm for the control equations adopted the SIMPLEC algorithm. The discrete method adopted the second-order upwind algorithm. The residual of the numerical calculation was set to 10^{-6}.

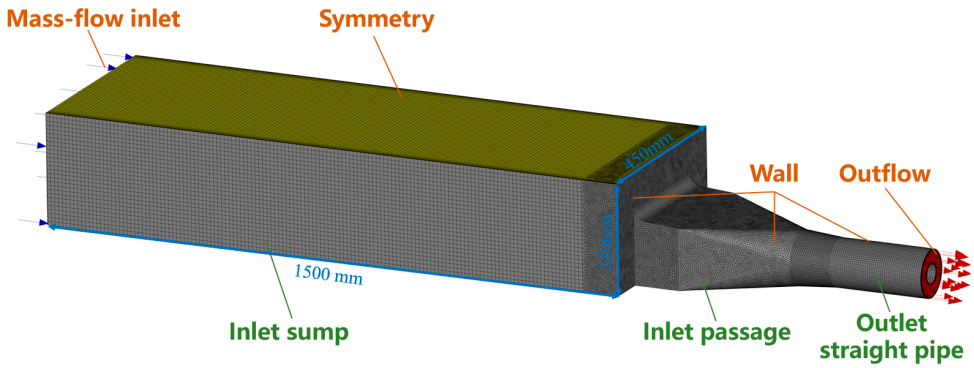

Figure 5. Boundary conditions and grid generation of calculation domains.

3.1.2. Grid Independence Analysis

To achieve a balance between computational accuracy and computational resource, a grid independence analysis was conducted on the inlet passage. According to previous research on the inlet passage [39,40], the initial number of grids was set to 0.8 million, and the number of grids added each time was 50% of the previous number of grids. The hydraulic loss of the inlet passage is an important indicator for measuring the hydraulic performance of the inlet passage, so it was selected for grid independence analysis. The hydraulic loss of inlet passage with six different grid numbers are shown in Table 1 and Figure 6. The calculation results indicate that with the increasing of the grid number, the loss-grid curve gradually decreases and tends to be horizontal. The relative error of hydraulic loss for grid numbers of 2.7 million and 4.05 million was 0.16% and less than 1%; therefore, the grid number of 2.7 million was selected as the grid for subsequent optimization calculations.

Table 1. Hydraulic loss of inlet passage with six different grid numbers.

Grid Number (Million)	0.8	1.2	1.8	2.7	4.05	6.08
Hydraulic loss (m)	0.0688	0.0657	0.0633	0.0624	0.0623	0.0622

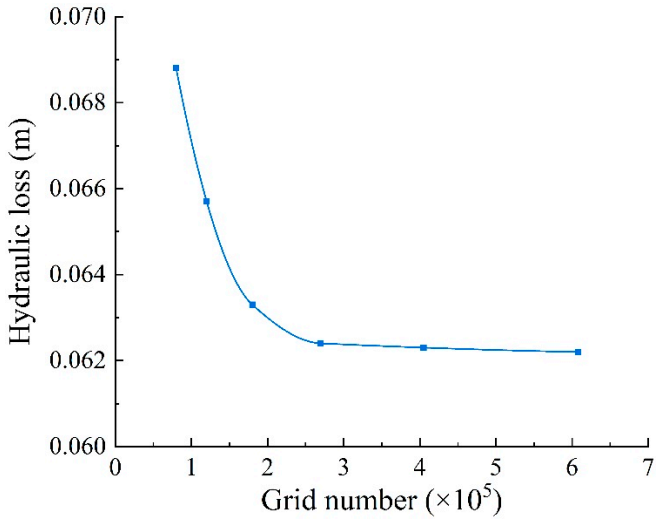

Figure 6. Relationship between hydraulic loss and grid number.

The grid generation of calculation domains is shown in Figure 5. In this research, the software completing the CFD calculations and simulations was Ansys Fluent, and the

finite volume method (FVM) was used in Ansys Fluent. The characteristics of the finite volumes are as follows: (1) The grids in the front and middle parts of the inlet sump and in outlet straight pipe are hexahedral grids with eight nodes. (2) The grids in the rear part of the inlet sump and in the inlet passage includes the prismatic grids with six nodes near the wall and tetrahedral grids with four or five nodes far from the wall. The type of turbulence in the inlet passage is mechanical turbulence, and it is caused by the friction of water flow with solid wall. The grid near the wall was densified, the distance between the first layer of grid and the wall was 0.4 mm, the number of prismatic layers used for the boundary layers was eight and the grid growth rate of prismatic layers was 1.2. The grid distribution is shown in Figure 7. The maximum skewness of the grid was 0.73, and the grid quality met the requirement of numerical calculation. For each fluid particle moving in three-dimensional space, the degrees of freedom were three [41].

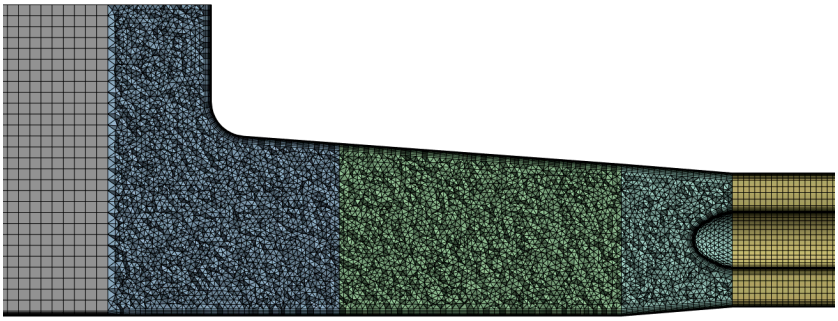

Figure 7. Grid distribution of computational domains.

3.2. Model Test

3.2.1. Model Test Rig Setup

The hydraulic performance of inlet passage was test in a model test rig. The model test rig is a vertical circulation system and relevant apparatuses are labeled in Figure 8. The vertical circulation system consisted of an inlet sump, an inlet passage, a water supply pump, an electromagnetic flowmeter, piezometers and pipes. The model of electromagnetic flowmeter is LDY-S and it was manufactured by Shanghai Guanghua Instrument Co. Ltd. The piezometer consists of a transparent rubber hose and a scale ruler. The inlet sump and inlet passage were made of transparent perspex, and it was convenient to observe the flow state of water. The flow rate in the circulation system was changed by adjusting the rotation speed of the water supply pump. The flow rate in the circulation system was measured by an electromagnetic flowmeter. The static pressure of water inside the pipe was measured through the piezometer. The relevant apparatuses of the circulation system were connected by pipes.

The inlet pressure measuring the cross-section was located 800 mm in front of the inlet cross-section of the inlet passage. The outlet pressure measuring the cross-section was located 200 mm behind the outlet cross-section of the inlet passage. According to Bernoulli's equation, the flow resistance of the inlet passage was calculated by the following formula.

$$\Delta h = \frac{1}{2g}\left(\overline{v_1}^2 - \overline{v_2}^2\right) + (H_1 - H_2) - \Delta h_{\mathrm{sp}} \tag{31}$$

where Δh is the hydraulic loss of inlet passage, $\overline{v_1}$ and $\overline{v_2}$ are, respectively, the average velocity of the inlet pressure measuring cross-section and outlet pressure measuring cross-section, H_1 and H_2 are, respectively, the piezometer heads of inlet pressure measuring cross-section and outlet pressure measuring cross-section and Δh_{sp} is the

hydraulic loss between the outlet cross-section of the inlet passage and outlet pressure measuring cross-section.

The uncertainty of flow rate measurement was ±0.5%. The uncertainty of static pressure measurement was ±0.94%. Thus, the total uncertainty of hydraulic loss of the inlet passage was ±1.06%, which meets the specification requirements [42].

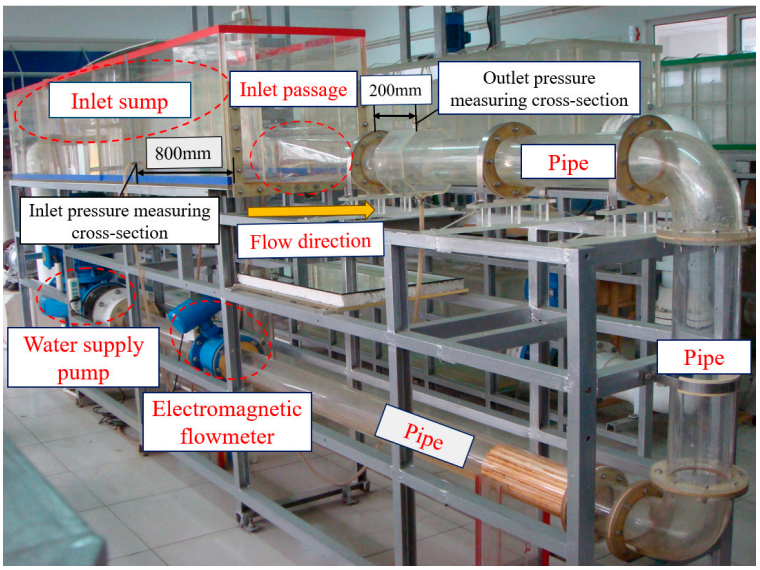

Figure 8. Photo of model test rig.

3.2.2. Model Test Result

Through the model test of the inlet passage, the hydraulic loss of the inlet passage was obtained to be 0.0620 m, and the photo of the flow state of the inlet passage model test is shown in Figure 9. The hydraulic loss of numerical simulation was 0.0624 m, the hydraulic loss between numerical simulation and model test was close and the relative error was 0.65%, which is less than 1%, indicating that the numerical calculation results of the inlet passage are reliable.

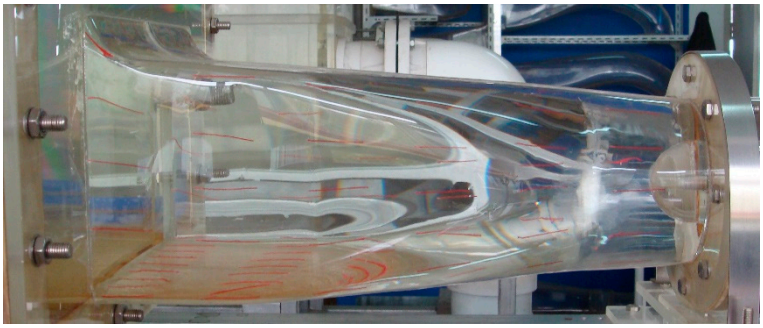

Figure 9. Photo of flow state of inlet passage.

4. Establishing Regression Model

4.1. Building Dataset

4.1.1. Formulating Calculation Scheme

Due to the contraction movement of the water flow in the inlet passage, the contraction angle has a significant impact on the hydraulic performance of the inlet passage [43]. Therefore, this paper selected three contraction angles including the contraction angle of the circular segment on the horizontal plane (θ_1), the contraction angle of the square to circular segment on the horizontal plane (θ_2) and the contraction

angle on the vertical plane (θ_3) as independent variables to explore their impact on the hydraulic performance of the inlet passage and search the optimal hydraulic performance inlet passage scheme. If the contraction angles of the inlet passage are too large, the zone near the sidewalls will produce flow separation, resulting in vortices and affecting the hydraulic performance of the inlet passage. In combination with the design requirements of the pump station [44], the subsequent optimization schemes will be adjusted according to the following constraints: ① the bottom surface of the square segment and the square to circular segment will be kept horizontal; ② the square segment length $l_1 \geq 120$mm; ③ the contraction angle of the circular segment on the horizontal plane $0^\circ \leq \theta_1 \leq 30^\circ$; ④ the contraction angle of the square to circular segment on the horizontal plane $20^\circ \leq \theta_2 \leq 70^\circ$; and ⑤ the contraction angle on the vertical plane $0^\circ \leq \theta_3 \leq 8^\circ$. On the basis of satisfying the constraint conditions, this paper made the inlet passage profile change uniformly in three-dimensional space as much as possible and perform a free combination of three factors and five levels for each factor to obtain 125 schemes. The numerical simulation calculations were performed on 125 schemes, and the calculation results of hydraulic performance of inlet passage were obtained.

4.1.2. Objective Function of Inlet Passage Hydraulic Performance

The hydraulic efficiency of the pump system is one of the core indicators to measure the hydraulic performance of the pump station. The inlet passage affects the hydraulic efficiency of the pump system from two aspects [45]. On the one hand, the smaller the hydraulic loss of the inlet passage is, the higher the hydraulic efficiency of the pump system is. On the other hand, the better the flow state at the outlet of the inlet passage is, the higher the hydraulic efficiency of the pump is, and the higher the hydraulic efficiency of the pump system is. Therefore, the hydraulic loss of the inlet passage, the uniformity of flow velocity distribution and the average angle of water flow entering the pump at the outlet cross-section of the inlet passage are usually selected as quantitative evaluation indicators for the hydraulic performance of the inlet passage [46]. This paper also selects these three evaluation indicators as objective functions.

Hydraulic loss is one of the important indicators for measuring the hydraulic performance of the inlet passage. A small hydraulic loss indicates a smooth flow state in the inlet passage, without flow separation and other adverse flow states. The calculation formula for hydraulic loss in the inlet passage is shown in (32), in which subscripts 1 and 2 represent the inlet and outlet cross-sections of the inlet passage, respectively.

$$h = z_1 - z_2 + \frac{\bar{p}_1}{\rho g} - \frac{\bar{p}_2}{\rho g} + \frac{\bar{u}_1^2}{2g} - \frac{\bar{u}_2^2}{2g} \tag{32}$$

where h is hydraulic loss, z_1 and z_2 are the elevation heads, $\bar{p}_1$ and $\bar{p}_2$ are the average pressure, u_1 and u_2 are the average velocity, ρ is water density and g is gravitational acceleration.

The uniformity of flow velocity distribution is used to measure the uniformity of flow velocity at the outlet cross-section of the inlet passage. The higher the uniformity of flow velocity distribution is, the better the inlet flow condition of the water pump is. The highest uniformity of flow velocity distribution is 100%. The formula for calculating the mass-weighted uniformity of flow velocity distribution is shown in (33).

$$V_u = \frac{\sum_{i=1}^{n}[(|v_{ai} - \bar{v}_{am}|)(|\rho \vec{v}_i A_i|)]}{|\bar{v}_{am}| \sum_{i=1}^{n}[(|\rho \vec{v}_i A_i|)]} \times 100\% \tag{33}$$

where V_u is uniformity of flow velocity distribution, i is the number of facets on the surface, n is the total number of facets on the surface, v_{ai} is axial flow velocity on the ith facet, $\bar{v}_{am}$ is the average flux of the axial flow velocity through the surface, $\vec{v}_i$ is the facet velocity vector on the ith facet and A_i is the facet area on the ith facet.

The average angle of water flow entering the pump is used to measure the direction of water flow movement at the outlet cross-section of the inlet passage. The closer the average angle of water flow entering the pump is to 90°, the better the inlet flow condition of the water pump is. The highest average angle of water flow entering the pump is 90°. The formula for calculating the mass-weighted average angle of water flow entering the pump is shown in (34).

$$\theta = \frac{\sum_{i=1}^{n}\left[\left(\left|90°-\arctan\left(\frac{v_{ti}}{v_{ai}}\right)\right|\right)(|\rho\vec{v}_i A_i|)\right]}{\sum_{i=1}^{n}[(|\rho\vec{v}_i A_i|)]} \tag{34}$$

where θ is average angle of water flow entering the pump and v_{ti} is projection velocity of resultant velocity on the ith facet.

4.1.3. Comprehensive Objective Function Based on the Information Weight Method

There are three evaluation indicators for the hydraulic performance of the inlet passage: hydraulic loss, uniformity of flow velocity distribution and average angle of water flow entering the pump. Based on previous research results [47], this paper adopted the information weight method to synthesize three objective functions into a comprehensive objective function. The weight of the information weight method is determined by quantifying the difference in evaluation objectives based on the amount of information distinguished by evaluation indicators. It can compare the advantages and disadvantages of different evaluation indicators and is used to handle multi-objective decision-making problems. It has the advantages of a simple method and calculation. The optimization problem in this paper has three objective functions X_k $(k = 1,2,3)$, with n $(n = 125)$ samples for each objective function, and X_{kj} $(j = 1,2,\cdots,n)$ represents the jth sample of the kth objective function. The steps to calculate the comprehensive objective function using the information weight method are as follows:

(1) Normalize the samples of each objective function by min-max normalization to obtain the three normalized objective functions samples X'_k, and X'_{kj} represents the jth sample of the kth objective function in the normalized samples.

$$X'_{kj} = \frac{X_{kj} - \left(X_{kj}\right)_{min}}{\left(X_{kj}\right)_{max} - \left(X_{kj}\right)_{min}} \tag{35}$$

(2) Calculate the mean value $\overline{X_k}$ and standard deviation S_k of the samples of each objective function.

$$\overline{X_k} = \frac{1}{n}\sum_{j=1}^{n} X'_{kj} \tag{36}$$

$$S_k = \sqrt{\frac{1}{n-1}\sum_{j=1}^{n}\left(X'_{kj} - \overline{X_k}\right)^2} \tag{37}$$

(3) Calculate the coefficient of variation V_k for the samples of each objective function.

$$V_k = S_k/\overline{X_k} \tag{38}$$

(4) Normalize the coefficient of variation to obtain the information weight W_k of samples of each objective function.

$$W_k = V_k/\sum_{k=1}^{3} V_k \tag{39}$$

(5) Calculate comprehensive objective function Y.

$$Y = W_1 \cdot (1 - X'_1) + W_2 \cdot X'_2 + W_3 \cdot X'_3 \tag{40}$$

In Equation (40), X'_1 represents the normalized hydraulic loss, X'_2 represents the normalized uniformity of flow velocity distribution and X'_3 represents the normalized

average angle of water flow entering the pump, W_1 represents the weight of normalized hydraulic loss, W_2 represents the weight of uniformity of flow velocity distribution and W_3 represents the weight of average angle of water flow entering the pump. The closer the comprehensive objective function (Y) is to 1, the better the hydraulic performance of the inlet passage.

4.2. Dataset

Numerical simulation calculations were conducted on 125 sets of inlet passage schemes to obtain corresponding hydraulic loss, uniformity of flow velocity distribution and the average angle of water flow entering the pump. Then, the comprehensive objective function values were calculated through the information weight method. The three contraction angles (θ_1, θ_2 and θ_3) and corresponding comprehensive objective function values (Y) of the inlet passage are shown in Figure 10, in which the larger the objective function value is, the larger the dot diameter is and the closer the dot color is to red.

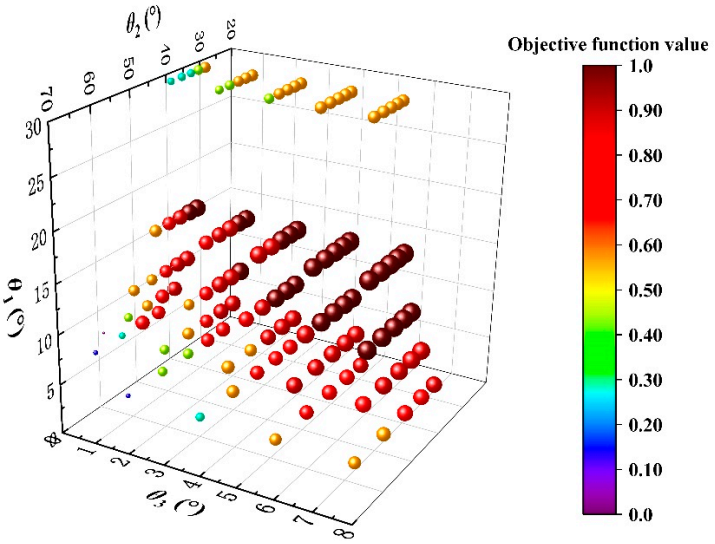

Figure 10. Contraction angles and comprehensive objective function values of inlet passage.

4.3. Hyperparameter Optimization

The hyperparameter is a manually configurable parameter that has already been set before machine learning. For the machine learning regression models, different hyperparameters lead to different learning performance, so hyperparameter optimization is a necessary task [48]. The hyperparameter optimization method used in this paper was Bayesian optimization, which is a probability-based optimization method and more efficient than the traditional grid search and random search method. In order to reduce the impact of randomness of splitting the dataset on the regression model and improve the generalization ability of the regression model, the method of splitting the dataset adopted the 10-fold cross validation method. Optimal hyperparameters of different regression models are listed in Table 2.

Table 2. Optimal hyperparameters of different regression models.

Regression Models	Types of Hyperparameters	Values
Gaussian Process Regression (GPR)	Sigma	0.463
	Basis function	0
	Kernel function	Isotropic squared exponential
	Kernel scale	856.26
	Standardize data	true
Feedforward Neural Network (FNN)	Number of fully connected layers	1
	First layer size	259
	Activation	Tanh
	Regularization strength	0.0007378
	Standardize data	True
Support Vector Regression (SVR)	Kernel function	Gaussian
	Box constraint	23.8196
	Kernel scale	4.3335
	Epsilon	0.0434
	Standardize data	true

4.4. Selecting Regression Model

To check the generalization ability of different regression models, the relationship between the predicted response and actual response of different regression models in the test set is shown in Figure 11. A perfect regression model has a predicted response equal to the true response, so all the points of perfect regression lie on a diagonal line. The vertical distance from the line to any point is the error of the prediction for that point. For the three regression models, the response points are randomly distributed on both sides of the diagonal line. When the response is closer to 1, the response error is smaller. When the response is around 0.5, the error is relatively larger. As a whole, the points of the GPR model were closer to the diagonal line than the points of the FNN and SVR model, which indicates that the GPR model has the minimum error and the best generalization ability.

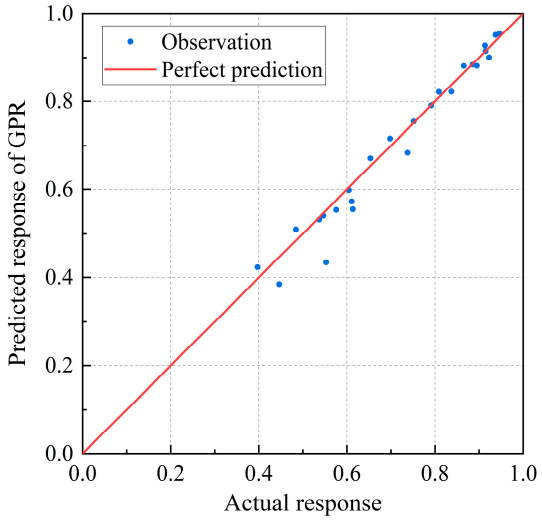

(**a**) GPR model

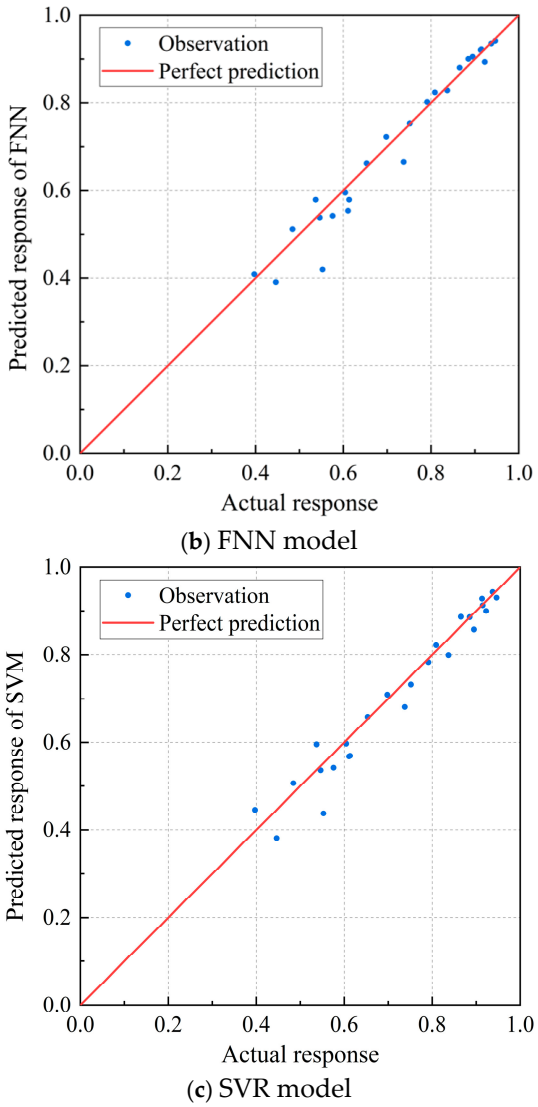

Figure 11. Relationship between predicted response and actual response of different regression models.

To quantify the generalization ability of different regression models, the coefficient of determination (R^2) was used. The closer the value of R^2 is to 1, the better the generalization ability of the model is. The R^2 values of different regression models are shown in Figure 12. The R^2 values of the GPR, FNN and SVR were, respectively, 0.958, 0.948 and 0.948 in the test set. The R^2 value of the GPR model was maximum in the test set during the three models, which indicates that the GPR model has the best predictive ability among the three regression models, so the GPR model was used in this paper to regress the three contraction angles (θ_1, θ_2 and θ_3) and comprehensive objective function (Y).

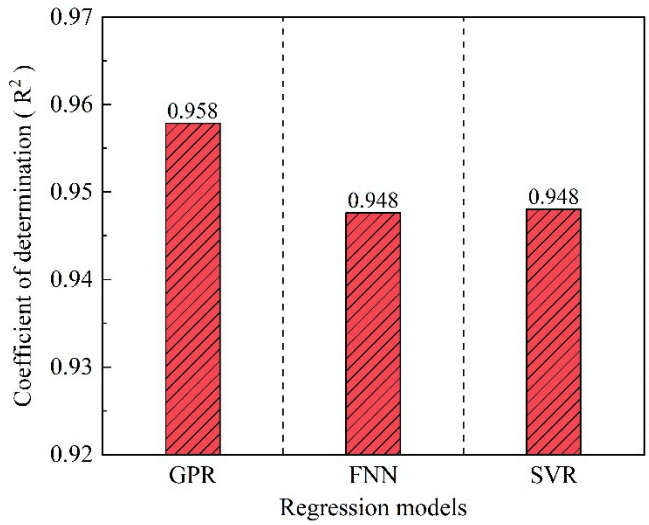

Figure 12. R^2 values of different regression models.

5. Sensitivity Analysis

To investigate the impact of different input parameters (contraction angles) on the output results (comprehensive objective function) of the GPR model, Sobol sensitivity analysis was conducted on the contraction angle parameters. The global sensitivity coefficient of the three contraction angles is shown in Figure 13. We can see that the ranking of first-order global sensitivity coefficient and total global sensitivity coefficient is $\theta_3 > \theta_2 > \theta_1$, which indicates that θ_3 had the greatest impact on the objective function value, followed by θ_2, and θ_1 had the smallest impact. For each contraction angle, the total global sensitivity coefficient was greater than the first order sensitivity coefficient, indicating that there was interaction between the three contraction angles.

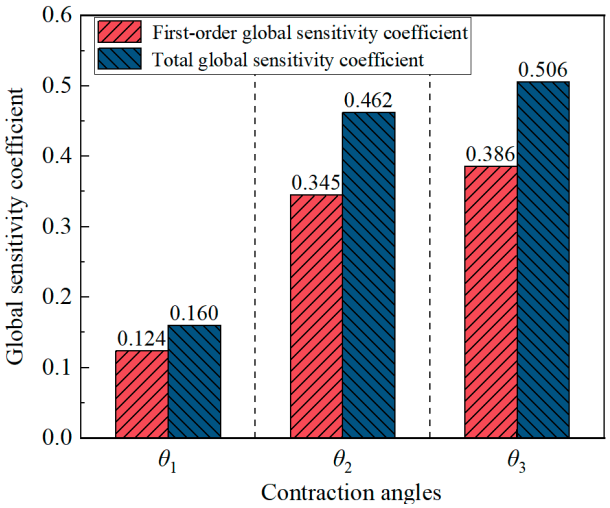

Figure 13. Global sensitivity coefficient of three contraction angles.

6. Genetic Algorithm Optimization

The genetic algorithm was used to search the optimal objective function value of the GPR model and corresponding contraction angles of the inlet passage. The parameter settings of genetic algorithm are listed in Table 3.

Table 3. Parameter settings of genetic algorithm.

Parameter Name	Population Size	Crossover Fraction	Migration Fraction	Fitness Tolerance
Value	50	0.8	0.2	10^{-6}

The variation in the three constraint angles and objective function values with generations is shown in Figure 14. We can see that with the increase in genetic generations, the objective function values gradually increased, and then the objective function values remained unchanged with the increase in genetic generations. In addition, the values of the three contraction angles remained unchanged with the increase in genetic generations. Finally, the maximum objective function value was 0.963 and the corresponding contraction angles were $\theta_1 = 13.34°$, $\theta_2 = 28.36°$and $\theta_3 = 3.64°$, respectively.

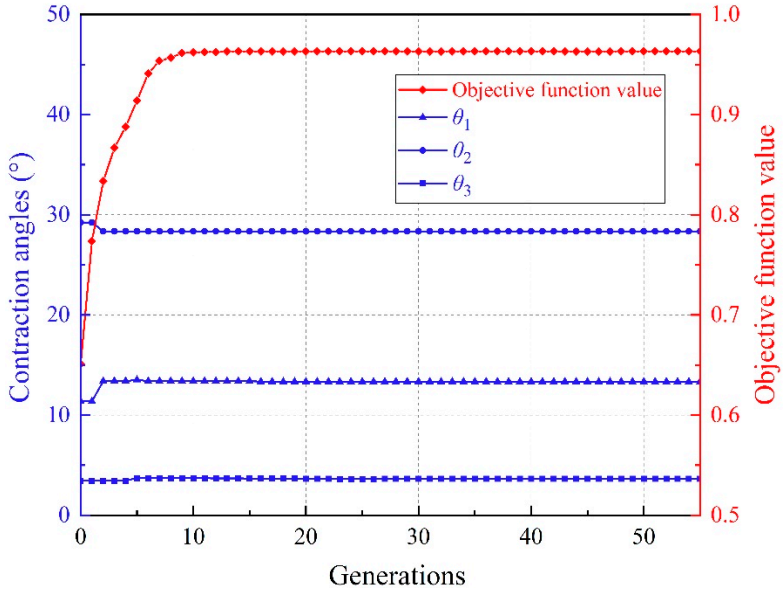

Figure 14. Variation in three constraint angles and objective function values with generations.

7. Numerical Simulation Results

7.1. CFD Verification of Optimal Scheme

Numerical simulation calculation was performed on the optimal scheme; the results are hydraulic loss h_{opt} =0.061 m, uniformity of flow velocity distribution V_{uopt}=99.10%, average angle of water flow entering the pump θ_{opt}=88.13° and objective function value Y_{opt}=0.953. The optimal objective function value obtained through the GPR model was 0.963; the relative error between the GPR model objective function value and the CFD objective function value was 1.0%, which indicates that the optimization results based on the GPR model are reliable.

7.2. Comparison of Numerical Simulation Results

7.2.1. Comparison of Hydraulic Performance Indicators

The values of various hydraulic performance indicators of the original scheme and optimal scheme are shown in Figure 15. We can see that the hydraulic loss h of the optimal scheme was 2.4% smaller than that of the original scheme, the uniformity of flow velocity distribution V_u of the optimal scheme was 0.1% larger than that of the original scheme, the average angle of water flow entering the pump θ of the optimal scheme was 0.2% smaller than that of the original scheme and, finally, the objective function value Y of the

optimal scheme was 8% larger than that of the original scheme, indicating that the hydraulic performance of the optimal scheme was better than that of the original scheme.

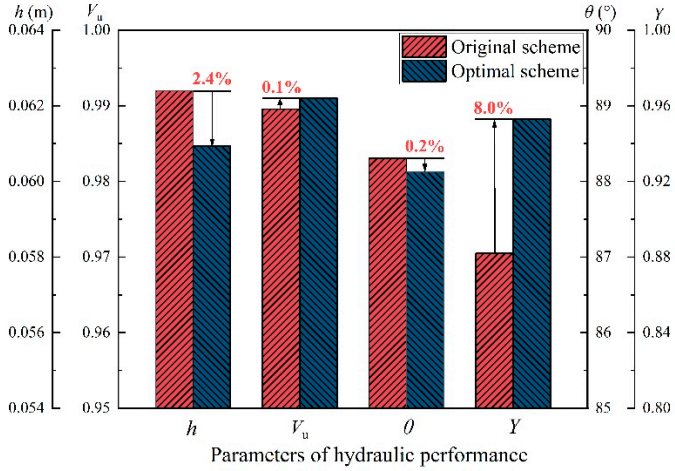

Figure 15. Values of various hydraulic performance indicators of original scheme and optimal scheme.

7.2.2. Location of Control Planes

In order to visually demonstrate the difference in interior characteristics between the original and optimal schemes, the distribution of velocity and the turbulent dissipation rate were displayed on plane 1 (Z = 0); the distribution of velocity was displayed on plane 2 (x = 0). Plane 1 and plane 2 are shown in Figure 16.

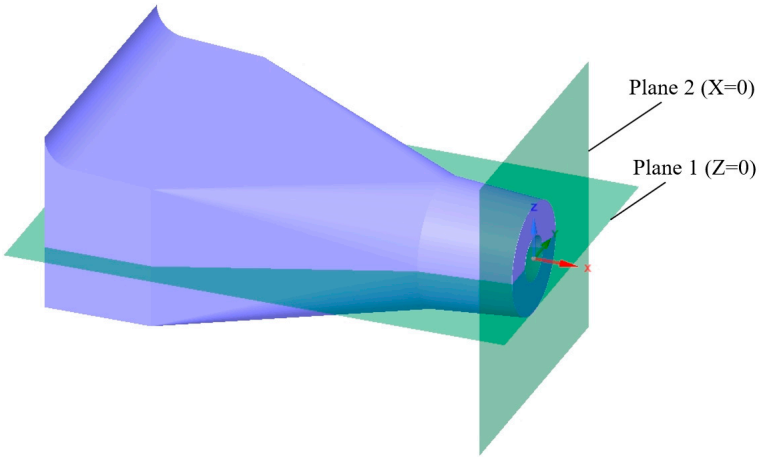

Figure 16. Location of control planes.

7.2.3. Comparison of Flow State

The flow state on plane 1 of the inlet passage of the original scheme and optimal scheme is shown in Figure 17. We can see that, for two schemes, the water flows into the inlet passage and the vortices are generated near the both side walls of the inlet section of inlet passage because of the separation of inlet flow. With the contraction of inlet passage, the vortices disappear and the flow velocity gradually increases. In summary, the flow state of the original scheme and optimal scheme is basically similar, and the main difference between the two schemes is that the vortex zone of the original scheme is larger than that of the optimal scheme, so it indicates that the flow state of the optimal scheme is better than that of the original scheme.

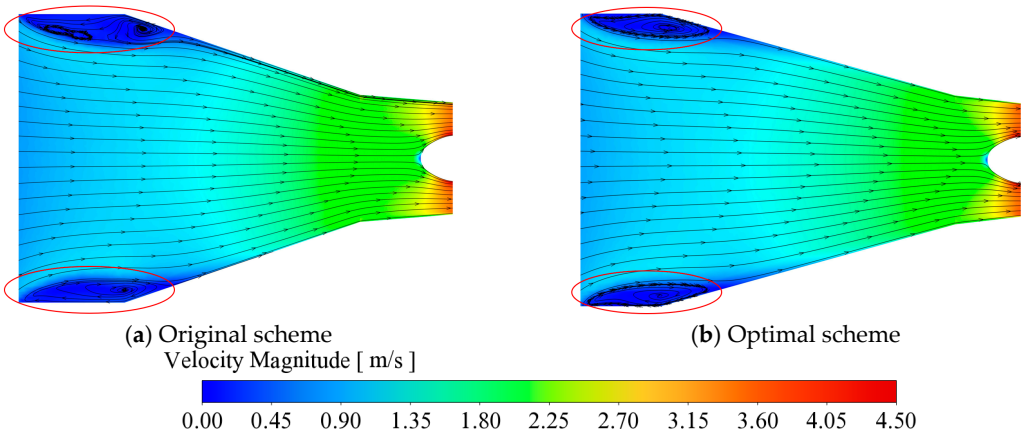

Figure 17. Flow state on plane 1 of inlet passage of original scheme and optimal scheme.

7.2.4. Comparison of Turbulent Dissipation Rate

The turbulent dissipation rate on plane 1 of the inlet passage of the original scheme and optimal scheme is shown in Figure 18. In the picture, the larger the turbulent dissipation rate is, the redder the color of the zone is, and the greater the hydraulic loss is. As can be seen from Figure 18, the larger hydraulic loss zones were mainly concentrated on both sides of the inlet section and near the side walls of the inlet passage because of the friction inside the vortex zones and the friction between the water flow and the inlet passage wall. By comparing the two pictures, the red zones at both sides of the inlet section and near the wall of the outlet section of the optimal scheme are smaller, so the hydraulic loss of the optimal scheme is smaller than the original scheme.

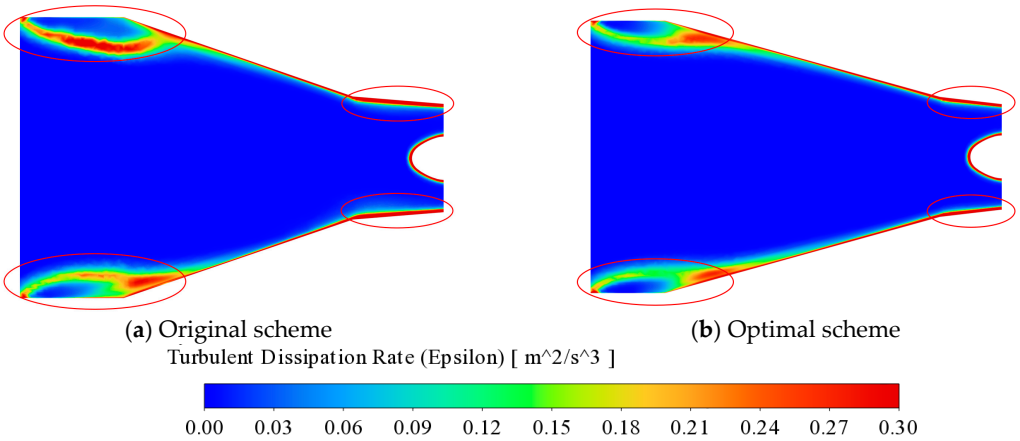

Figure 18. Turbulent dissipation rate on plane 1 of inlet passage of original scheme and optimal scheme.

7.2.5. Comparison of Velocity Distribution

Velocity distribution on plane 2 of the inlet passage of the original scheme and optimal scheme is shown in Figure 19. The more uniform the velocity distribution is, the better the flow state of the pump inlet is. As can be seen from Figure 19, for both schemes, the flow velocity was distributed in an annular pattern from low to high along the outer ring to the inner ring on plane 2, and the main difference between the two schemes is that there are the local low-speed zones in the lower part on plane 2 of the original scheme, so the flow state on plane 2 of the optimal scheme is better than the original scheme.

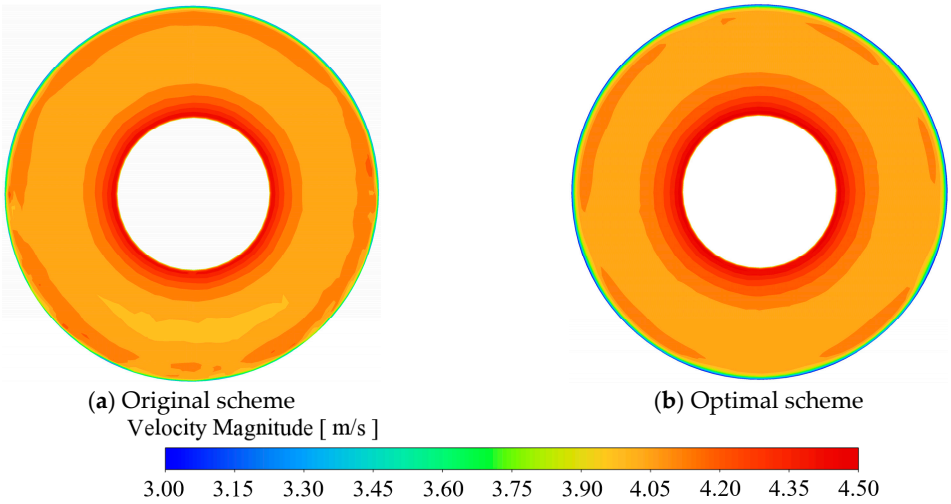

Figure 19. Velocity distribution on plane 2 of inlet passage of original scheme and optimal scheme.

8. Conclusions

(1) Three machine learning regression models (GPR, FNN and SVR) were used to regress the relationship between the three contraction angles (θ_1, θ_2 and θ_3) of the inlet passage and the comprehensive objective function (Y). By using the Bayesian optimization algorithm and 10-fold cross validation method to perform hyperparameter optimization on three regression models, the coefficients of determination (R^2) of the three optimized models were compared, and the order of R^2 of the three regression models in the test set from large to small was as follows: $R^2_{\mathrm{GPR}} > R^2_{\mathrm{FNN}} = R^2_{\mathrm{SVR}}$. The GPR model had the highest R^2 in the test set, indicating its strongest generalization ability. Therefore, the GPR model was selected as the regression model for this study.

(2) To investigate the impact degree of different input parameters (contraction angles) on the output results (objective function) of the GPR model, Sobol sensitivity analysis was conducted on the contraction angle parameters. The rankings of the first-order global sensitivity coefficient and total global sensitivity coefficient were both $\theta_3 > \theta_2 > \theta_1$, which indicated that θ_3 had the greatest impact on the objective function value, followed by θ_2, and θ_1 had the smallest impact. In addition, for each contraction angle, the total global sensitivity coefficient was greater than the first-order sensitivity coefficient, indicating that there is interaction between different contraction angles.

(3) The genetic algorithm was used to search the optimal objective function value of the GPR model. The maximum comprehensive objective function value was 0.963 and the corresponding three contraction angles were $\theta_1 = 13.34°$, $\theta_2 = 28.36°$ and $\theta_3 = 3.64°$, respectively. The comprehensive objective function value of the optimal scheme was 8% larger than that of the original scheme, indicating that the hydraulic performance of the optimal scheme is better than that of the original scheme. From the perspective of the flow state and turbulent dissipation rate on plane 1 of the inlet passage and velocity distribution uniformity on plane 2 of the inlet passage, the reasons why the hydraulic performance of the optimal scheme is superior to the original scheme were analyzed. The results of this study can provide reference for the optimization of inlet passages of coastal drainage pump systems.

Author Contributions: T.J.: Conceptualization, Methodology, Software, Data curation, Visualization, Formal analysis, Funding acquisition, Writing—original draft. W.L.: Project administration, Funding acquisition, Writing—review and editing. L.L.: Validation, Data curation, Writing—review and editing. L.X.: Data curation, Funding acquisition, Writing—review and editing. W.X.: Software, Funding acquisition, Writing—review and editing. J.L.: Software, Writing—

review and editing. Y.Z.: Visualization, Writing—review and editing. All authors have read and agreed to the published version of the manuscript.

Funding: This research was funded by the Postgraduate Research & Practice Innovation Program of Jiangsu Province grant number KYCX23_3542, Research and Development Project of Jiangsu South to North Water Diversion Technology of China grant number JSNSBD202302, Water Conservancy Technology Foundation of Jiangsu Provincial of China grant number 2020060, Jiangsu South-to-North Water Diversion Technology R&D Project grant number JSNSBD202105, Jiangsu Water Conservancy Science and Technology Project grant number 2022010, Open Project of Jiangsu Province High Efficiency and Energy saving Large Axial Flow Pump Station Engineering Research Center in 2022 grant number ECHEAP027, High-tech Key Laboratory of Agricultural Equipment and Intelligence of Jiangsu Province and College of Agricultural Engineering, Jiangsu University.

Institutional Review Board Statement: Not applicable.

Informed Consent Statement: Not applicable.

Data Availability Statement: All data generated or analyzed during this study are included in this manuscript file.

Conflicts of Interest: The authors declare that they have no known competing financial interests or personal relationships that could have appeared to influence the work reported in this paper.

Abbreviations

Abbreviation	Definition
AI	Artificial Intelligence
CFD	Computational Fluid Dynamics
FNN	Feedforward Neural Network
GA	Genetic Algorithm
GP	Gaussian Process
GPR	Gaussian Process Regression
KKT	Karush–Kuhn–Tucker
ML	Machine Learning
PAT	Pump As Turbine
RNG	Re-normalization Group
SVR	Support Vector Regression
SVM	Support Vector Machine
TLV	Tip Leakage Vortex
Y	Comprehensive Objective Function

References

1. Zhang, X.W.; Tang, F.P. Energy loss evaluation of axial flow pump systems in reverse power generation operations based on entropy production theory. *Sci. Rep.* **2022**, *12*, 8667. https://doi.org/10.1038/s41598-022-12667-7.
2. Han, W.; Liu, Y.; Gong, C.Y.; Su, Y.L.; Guo, P.Y.; Su, M.; Shi, F.X.; Wei, Z.Z. Effect of tip clearance on performance of contra-rotating axial flow water-jet propulsion pump. *Mod. Phys. Lett. B* **2020**, *34*, 2050094. https://doi.org/10.1142/S0217984920500943.
3. Xu, L.; Lu, L.G.; Chen, W.; Wang, G. Flow pattern analysis on inlet and outlet conduit of shaft tubular pump system of Pizhou pumping station in South-to-North Water Diversion Project. *Trans. Chin. Soc. Agric. Eng.* **2012**, *28*, 50–56. https://doi.org/10.3969/j.issn.1002-6819.2012.06.009. (In Chinese)
4. Ruan, F.X.; Lv, J.X. Experimental study on prevention and dissipation of vortex for Donghe drainage pump station inlet duct. *Drain. Irrig. Mach.* **2002**, *3*, 3. https://doi.org/10.3969/j.issn.1674-8530.2002.03.007. (In Chinese)
5. Lu, L.G. *Optimum Hydraulic Design for High Performance Large Pump System with Low Head*, 1st ed.; China Water & Power Press: Beijing, China, 2013. (In Chinese)
6. Zhang, X.W.; Tang, F.P. Investigation on hydrodynamic characteristics of coastal axial flow pump system model under full working condition of forward rotation based on experiment and CFD method. *Ocean. Eng.* **2022**, *253*, 111286. https://doi.org/10.1016/j.oceaneng.2022.111286.

7. Kan, K.; Zhao, F.; Xu, H.; Feng, J.G.; Chen, H.X.; Liu, W.D. Energy performance evaluation of an axial-flow pump as turbine under conventional and reverse operating modes based on an energy loss intensity model. *Phys. Fluids* **2023**, *35*, 015125. https://doi.org/10.1063/5.0132667.
8. Zharkovskii, A.; Svoboda, D.; Borshchev, I.; Klyuyev, A.; Ivanov, E.; Shutsky, S. Axial-flow pump with enhanced cavitation erosion resistance. *Energies* **2023**, *16*, 1344. https://doi.org/10.3390/en16031344.
9. Jia, X.Q.; Zhang, S.K.; Zhu, Z.C. Research on blade tip clearance cavitation and turbulent kinetic energy characteristics of axial flow pump based on the partially-averaged Navier-Stokes model. *J. Hydrodyn.* **2024**, *36*, 184–201. https://doi.org/10.1007/s42241-024-0014-x.
10. Shi, L.J.; Yuan, Y.; Jiao, H.F.; Tang, F.P.; Cheng, L.; Yang, F.; Jin, Y.; Zhu, J. Numerical investigation and experiment on pressure pulsation characteristics in a full tubular pump. *Renew. Ene*rgy **2021**, *163*, 987–1000. https://doi.org/10.1016/j.renene.2020.09.003.
11. Yang, F.; Chang, P.C.; Hu, W.Z.; Mao, B.B.; Liu, C.; Li, Z.B. Numerical study on pressure pulsation in a slanted axial-flow pump device under partial loads. *Processes* **2021**, *9*, 1404. https://doi.org/10.3390/pr9081404.
12. Song, X.J.; Liu, C. Experimental investigation of pressure pulsation induced by the floor-attached vortex in an axial flow pump. *Adv. Mech. Eng.* **2019**, *11*, 1–13. https://doi.org/10.1177/1687814019838708.
13. Zhang, W.P.; Tang, F.P.; Shi, L.J.; Hu, Q.J.; Zhou, Y. Effects of an inlet vortex on the performance of and axial-flow pump. *Energies* **2020**, *13*, 2854. https://doi.org/10.3390/en13112854.
14. Ghorani, M.M.; Haghighi, M.H.S.; Maleki, A.; Riasi, A. A numerical study on mechanisms of energy dissipation in a pump as turbine (PAT) using entropy generation theory. *Renew. Energy* **2020**, *162*, 1036–1053. https://doi.org/10.1016/j.renene.2020.08.102.
15. Yu, H.; Wang, T.; Dong, Y.C.; Gou, Q.Q.; Lei, L.; Liu, Y.Q. Numerical investigation of splitter blades on the performance of a forward-curved impeller used in a pump as turbine. *Ocean. Eng.* **2023**, *281*, 114721. https://doi.org/10.1016/j.oceaneng.2023.114721.
16. Ji, L.L.; Li, W.; Shi, W.D.; Chang, H.; Yang, Z.Y. Energy characteristics of mixed-flow pump under different tip clearances based on entropy production analysis. *Energy* **2020**, *199*, 117447. https://doi.org/10.1016/j.energy.2020.117447.
17. Zhou, L.; Huang, J.W.; Bai, L.; Krzemianowski, Z.; El-Emam, M.A.; Yasser, E.; Agarwal, R. Application of entropy production theory for energy losses and other investigation in pumps and turbines: A review. *Appl. Energy* **2022**, *318*, 119211. https://doi.org/10.1016/j.apenergy.2022.119211.
18. Rezvaya, K.; Krupa, E.; Shudryk, A.; Drankovskiy, V. Solving the hydrodynamical tasks using CFD programs. In Proceedings of the International Conference on Intelligent Energy and Power Systems, Kharkiv, Ukraine, 10–14 September 2018; pp. 205–209.
19. Simão, M.; Pérez-Sánchez, M.; Carravetta, A.; López-Jiménez, P.; Ramos, H.M. Velocities in a Centrifugal PAT Operation: Experiments and CFD Analyses. *Fluids* **2018**, *3*, 3. https://doi.org/10.3390/fluids3010003.
20. Wang, L.; Tang, F.P.; Liu, H.Y.; Zhang, X.W.; Sun, Z.Z.; Wang, F. Investigation of cavitation and flow characteristics of tip clearance of bidirectional axial flow pump with different clearances. *Ocean. Eng.* **2023**, *288*, 115960. https://doi.org/10.1016/j.oceaneng.2023.115960.
21. Jin, Y.; He, X.K.; Zhang, Y.; Zhou, S.S.; Chen, H.C.; Liu, C. Numerical and experimental investigation of external characteristics and pressure fluctuation of a submersible tubular pumping system. *Processes* **2019**, *7*, 949. https://doi.org/10.3390/pr7120949.
22. Kan, K.; Zhang, Q.Y.; Xu, H.; Feng, J.G.; Song, Z.G.; Cheng, J.P.; Binama, M. Investigation of non-uniform inflow effects on impeller forces in axial-flow pumps operating as turbines. *Water* **2024**, *16*, 1428. https://doi.org/10.3390/w16101428.
23. Zhang, X.W.; Tang, F.P.; Chen, Y.T.; Huang, C.B.; Chen, Y.J.; Wang, L.; Shi, L.J. Experimental study on the internal pressure pulsation characteristics of a bidirectional axial flow pump operating in forward and reverse directions. *Machines* **2022**, *10*, 167. https://doi.org/10.3390/machines10030167.
24. Wang, B.; Wang, J.T. Application of artificial intelligence in computational fluid dynamics. *Ind. Eng. Chem. Res.* **2021**, *60*, 2772–2790. https://doi.org/10.1021/acs.iecr.0c05045.
25. Huang, L.; Zou, J.J.; Liu, B.Q.; Jin, Z.J.; Qian, J.Y. Machine learning assisted microchannel geometric optimization—A case study of channel designs. *Energies* **2024**, *17*, 44. https://doi.org/10.3390/en17010044.
26. Sun, Z.Z.; Tang, F.P.; Shi, L.J.; Liu, H.Y. Multi-Conditional optimization of a high-specific-speed axial flow pump impeller based on machine learning. *Machines* **2022**, *10*, 1037. https://doi.org/10.3390/machines10111037.
27. Kan, K.; Zhou, J.; Feng, J.G.; Xu, H.; Zheng, Y.; Chen, H.X.; Chen, J.B. Intelligent optimization of axial-flow pump using physics-considering machine learning. *J. Comput. Des. Eng.* **2024**, *11*, 325–342. https://doi.org/10.1093/jcde/qwae013.

28. Ping, X.; Yang, F.B.; Zhang, H.G.; Zhang, J.; Zhang, W.J.; Song, G.G. Introducing machine learning and hybrid algorithm for prediction and optimization of multistage centrifugal pump in an ORC system. *Energy* **2021**, *222*, 120007. https://doi.org/10.1016/j.energy.2021.120007.
29. Zhao, J.T.; Pei, J.; Yuan, J.P.; Wang, W.J. Structural optimization of multistage centrifugal pump via computational fluid dynamics and machine learning method. *J. Comput. Des. Eng.* **2023**, *10*, 1204–1218. https://doi.org/10.1093/jcde/qwad045.
30. Li, W.; Huang, Y.X.; Ji, L.L.; Ma, L.L.; Agawal, R.K.; Awais, M. Prediction model for energy conversion characteristics during transient processes in a mixed-flow pump. *Energy* **2023**, *290*, 130260. https://doi.org/10.1016/j.energy.2023.127082.
31. Li, W.; Long, Y.; Ji, L.L.; Li, H.M.; Li, S.; Chen, Y.F.; Yang, Q.Y. Effect of circumferential spokes on the rotating stall flow field of mixed-flow pump. *Energy* **2024**, *290*, 130260. https://doi.org/10.1016/j.energy.2024.130260.
32. Zhao, X.T.; Zhang, D.S.; Zhang, R.H.; Xu, B. A comparative study of Gaussian process regression with other three machine learning approaches in the performance prediction of centrifugal pump. *J. Mech. Eng. Sci.* **2021**, *236*, 3938–3949. https://doi.org/10.1177/09544062211050542.
33. Tang, S.N.; Zhu, Y.; Yuan, S.Q. Intelligent fault identification of hydraulic pump using deep adaptive normalized CNN and synchrosqueezed wavelet transform. *Reliab. Eng. Syst. Saf.* **2022**, *224*, 108560. https://doi.org/10.1016/j.ress.2022.108560.
34. Zhang, F.F.; Tao, R.; Zhu, D.; Wu, Y.Z.; Jin, F.Y.; Xiao, R.F. Anti-cavitation leading-edge profile design of centrifugal pump impeller blade based on genetic algorithm and decision tree. *J. Braz. Soc. Mech. Sci. Eng.* **2022**, *44*, 279. https://doi.org/10.1007/s40430-022-03528-5.
35. Shin, J.H.; Cho, Y.H. Machine-Learning-Based coefficient of performance prediction model for heat pump systems. *Appl. Sci.* **2022**, *12*, 362. https://doi.org/10.3390/app12010362.
36. Chen, Y.; Kong, G.Q.; Xu, X.L.; Hu, S.J.; Yang, Q. Machine-learning-based performance prediction of the energy pile heat pump system. *J. Build. Eng.* **2023**, *77*, 107442. https://doi.org/10.1016/j.jobe.2023.107442.
37. Wang, W.J.; Wang, Y. Analysis of inner flow in low specific speed centrifugal pump based on, L.E.S. *J. Mech. Sci. Technol.* **2013**, *27*, 1619–1626. https://doi.org/10.1007/s12206-013-0408-0.
38. Wang, L.; Liu, H.L.; Wang, K.; Zhou, L.; Jiang, X.P.; Li, Y. Numerical simulation of the sound field of a five-stage centrifugal pump with different turbulence models. *Water* **2019**, *11*, 1777. https://doi.org/10.3390/w11091777.
39. Zhang, W.P.; Shi, L.J.; Tang, F.P.; Duan, X.H.; Liu, H.Y.; Sun, Z.Z. Analysis of inlet flow passage conditions and their influence on the performance of an axial-flow pump. *J. Power Energy* **2020**, *235*, 733–746. https://doi.org/10.1177/0957650920957475.
40. Yang, F.; Li, Z.B.; Yuan, Y.; Liu, C.; Zhang, Y.Q.; Jin, Y. Numerical and experimental investigation of internal flow characteristics and pressure fluctuation in inlet passage of axial flow pump under deflection flow conditions. *Energies* **2021**, *14*, 5245. https://doi.org/10.3390/en14175245.
41. Banaszek, A.; Łosiewicz, Z.; Jurczak, W. Corrosion influence on safety of hydraulic pipelines installed on decks of contemporary product and chemical tankers. *Pol. Marit. Res.* **2018**, *25*, 71–77. https://doi.org/10.2478/pomr-2018-0056.
42. Tao, Y.J.; Wu, J.B.; Wang, W.L.; Zhao, C.P.; Liu, W.W.; Wang, L.; Pan, Z.B.; Miu, F.M.; Wang, J.B.; Song, Q.S.; et al. *Rotodynamic Pumps—Hydraulic Performance Acceptance Tests—Grades 1, 2 and 3*; China Planning Press: Beijing, China, 2016. (In Chinese)
43. Zhang, G.Y.; Zhi, Y.F.; Zhu, R.S.; Lin, B.; Fu, Q. Research on optimum design of inlet channel of seawater circulating pump in nuclear power plant. *J. Xihua Univ.* **2024**, *43*, 80–88. doi: 10.12198/j.issn.1673 − 159X.4982.
44. Lu, Z.M.; Zhu, L.J.; Huang, Y.L.; Hu, D.Y.; Li, D.M.; Bei, D.P.; Yang, J.Y.; Huang, Y.; Wu, J.; Zhu, Q.H.; et al. *Standard for Pumping Station Design*, 1st ed.; China Planning Press: Beijing, China, 2022. (In Chinese)
45. Xu, L.; Lu, L.G.; Wang, H.; Li, Y.N. Influence of control size of shaft inlet conduit on hydraulic performance. *Hydro-Sci. Eng.* **2014**, *5*, 47–52. https://doi.org/10.16198/j.cnki.1009-640x.2014.05.004.
46. Jiao, W.X.; Cheng, L.; Zhang, D.; Zhang, B.W.; Su, Y.P.; Wang, C. Optimal design of inlet passage for waterjet propulsion system based on flow and geometric parameters. *Adv. Mater. Sci. Eng.* **2019**, *2019*, 2320981. https://doi.org/10.1155/2019/2320981.
47. Li, Z.X.; Feng, J.G.; Qian, S.T.; Xu, H. Optimization of rectification bottom sill parameters in drainage pumping stations. *Trans. Chin. Soc. Agric. Eng.* **2021**, *37*, 56–63. https://doi.org/10.11975/j.issn.1002-6819.2021.03.007. (In Chinese)
48. Zhu, Y.; Zhou, T.; Tang, S.N.; Yuan, S.Q. A data-driven diagnosis scheme based on deep learning toward fault identification of the hydraulic piston pump. *J. Mar. Sci. Eng.* **2023**, *11*, 1273. https://doi.org/10.3390/jmse11071273.